JACS
JOURNAL OF THE AMERICAN CHEMICAL SOCIETY
Article
pubs.acs.org/JACS

A Functionally Stable Manganese Oxide Oxygen Evolution Catalyst in Acid

Michael Huynh,[†,‡] D. Kwabena Bediako,[†] and Daniel G. Nocera*[,†]

[†]Department of Chemistry and Chemical Biology, Harvard University, Cambridge, Massachusetts 02138, United States
[‡]Department of Chemistry, Massachusetts Institute of Technology, Cambridge, Massachusetts 02139, United States

Supporting Information

ABSTRACT: First-row metals have been a target for the development of oxygen evolution reaction (OER) catalysts because they comprise noncritical elements. We now report a comprehensive electrochemical characterization of manganese oxide (MnOx) over a wide pH range, and establish MnOx as a functionally stable OER catalyst owing to self-healing, is derived from MnOx redeposition that offsets catalyst dissolution during turnover. To study this process in detail, the oxygen evolution mechanism of MnOx was investigated electrokinetically over a pH range spanning acidic, neutral, and alkaline conditions. In the alkaline pH regime, a ~60 mV/decade Tafel slope and inverse first-order dependence on proton concentration were observed, whereas the OER acidic pH regime exhibited a quasi-infinite Tafel slope and zeroth-order dependence on proton concentration. The results reflect two competing mechanisms: a one-electron one-proton PCET pathway that is dominant under alkaline conditions and a Mn^{3+} disproportionation process, which predominates under acidic conditions. Reconciling the rate laws of these two OER pathways with that of MnOx electrodeposition elucidates the self-healing characteristics of these catalyst films. The intersection of the kinetic profile of deposition and that of water oxidation as a function of pH defines the region of kinetic stability for MnOx and importantly establishes that a non-noble metal oxide OER catalyst may be operated in acid by exploiting a self-healing process.

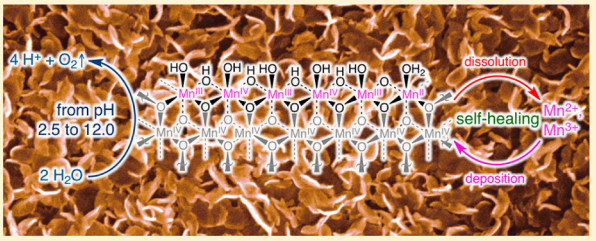

1. INTRODUCTION

Solar-driven electrochemical splitting of water to hydrogen and oxygen affords a method to store renewable energy in the form of energy-dense chemical fuels on a scale commensurate with future global energy requirements.[1−6] Of the two half reactions for water splitting, the oxygen evolution reaction (OER) is more kinetically demanding because it requires the coupled transfer of four protons and four electrons from two water molecules[7,8] to release one oxygen molecule.[9,10] The most active OER catalysts comprise "critical" elements that are expensive and lack sufficient abundance to be utilized on a global scale;[5,11] performing OER with commensurate activity by using noncritical elements remains a significant challenge. Discovery paths to noncritical OER catalysts follow two disparate approaches: "top−down" experimental and computational screening for mixed metal oxides[12−15] and a "bottom−up" experimental approach focused on defining the structure and mechanism of unary metal oxides to guide catalyst discovery.[16,17] Adopting the latter methodology with knowledge of the rate laws for catalyst formation (including nucleation and steady-state growth) and turnover, we have shown that conditions may be chosen to achieve promising oxygen evolution activity in neutral and near neutral pH electrolytes by exploiting the self-healing ability of catalysts.[18,19]

Our ability to operate OER catalysts at neutral and near neutral pH electrolytes has enabled our construction of buried junction devices (e.g., the artificial leaf) from noncritical materials.[20,21] To attain appreciable solar-to-fuels efficiencies, the combination of PV, catalyst, and electrolyte requires precise optimization. As described with equivalent circuit analysis,[22] the $j-V$ curves of the PV material and catalyst must be matched for maximizing operating power. Moreover, the stability of different photovoltaic materials vary in different pH regimes and thus provides an imperative to further extend the operation of OER catalysts over wider pH ranges, from basic and neutral to acidic pH regimes. For example, silicon is quickly passivated to silicon dioxide in alkaline media, which necessitates the use of catalysts that are stable in low to moderate pH electrolytes if the catalyst is to be directly integrated with silicon. Late first-row transition metal oxides, such as the Co−OEC,[23,24] Ni−OEC,[25,26] and more conventional "basic" oxides (e.g., from groups I and II elements),[16,17] are not stable in acidic conditions where such catalysts are known to corrode quickly. In contrast, early first-row transition metal oxides are resistant to corrosion in acidic environments and indeed have been used to passivate other more susceptible metal surfaces.[27] Thus, we turned our attention to defining activity profiles of early transition metal oxides and, in particular, to an electrodeposited manganese oxide catalyst (henceforth denoted MnOx). Manganese oxide-based materials have been examined extensively in neutral and basic solutions.[28−40] However, the

Received: January 12, 2014
Published: March 26, 2014

   dx.doi.org/10.1021/ja413147e | J. Am. Chem. Soc. 2014, 136, 6002−6010

OER activity of manganese oxides has garnered less attention in acidic pH regimes.[41−47] We now extend the understanding of oxidic manganese OER catalysts by elucidating the mechanism of MnOx under a wide pH range with detailed electrokinetics measurements. Tafel and reaction order analysis suggest two distinct OER pathways for MnOx: one prevalent in acidic and the other in alkaline electrolyte conditions. The rate laws of these water oxidation mechanisms are unified with that of catalyst deposition to elucidate the functional stability of MnOx films during OER catalysis, thus enabling us to predict and quantify the self-healing nature of MnOx in acid, a pH regime that hitherto has remained largely undefined for OER catalysts comprising noncritical elements. From this knowledge, we show that a metal oxide OER catalyst may operate with facility in acid, a realm previously dominated by oxides of iridium and ruthenium.

2. EXPERIMENTAL SECTION

2.1. Materials. $MnCl_2{\cdot}4H_2O$ (99.995% trace metals basis, Strem), KOH (88%, Macron), and KNO_3 (99.0−100.5%, Macron) were used as received. Methylphosphonic acid (98%, Aldrich) was recrystallized twice from boiling acetonitrile (HPLC grade, Aldrich). Phosphoric acid (85 wt % in H_2O, 99.99% trace metals basis, Aldrich) was used as received. Type I water (EMD Millipore, 18.2 MΩ cm resistivity) was exclusively used to rinse electrodes and glassware as well as to prepare solutions.

2.2. Solution Preparation. Mn^{2+}-free solutions of phosphate (P_i) were prepared by diluting stock phosphoric acid (85 wt % in H_2O, ∼14.6 M) with reagent water. Additional KNO_3 was added to maintain the ionic strength (μ) of the solution at ∼2 M, which mitigated diffuse double layer effects.[48] Solution pH was adjusted by adding pellets of solid KOH and aliquots of concentrated KOH while monitoring with a pH meter (VWR).

2.3. General Electrochemical Methods. All electrochemical experiments were conducted using a CH Instruments 760D bipotentiostat, a BASi Ag/AgCl reference electrode (filled with saturated KCl), and a Pt-mesh counterelectrode. All measurements were performed using a three-electrode electrochemical cell with a porous glass frit separating the working and auxiliary compartments. Glassware and cells were cleaned by soaking in aqua regia and rinsing with reagent water. All procedures were performed at ambient temperature (23 ± 1 °C), and electrode potentials were converted to the NHE scale using $E(\mathrm{HE}) = E(\mathrm{Ag/AgCl}) + 0.197$ V. All overpotentials for the oxygen evolution reaction (OER) from H_2O were computed using $\eta = E(\mathrm{NHE}) - 0.059\ \mathrm{V} \times \mathrm{pH}$.

Unless otherwise specified, OER studies employed working electrodes of fluorine-doped, tin oxide-coated glass (FTO) with 7 Ω/sq surface resistivity (TEC-7) purchased as precut 1 cm × 2.5 cm pieces from Hartford Glass. FTO slides were sonicated in acetone and rinsed with reagent water prior to use. A 1 cm^2 electrode area was created by using a 0.5 cm wide strip of Scotch tape as a mask. Rotating disk electrode (RDE) experiments employed a Pine Instruments MSR rotator with a 0.196 cm^2 Pt-disk rotating electrode, polished to mirror shine with 0.05 μm alumina (CH Instruments) and cycled ∼50 times at 300 mV/s from −0.2 to 1.5 V in 0.5 M H_2SO_4 (99.999% trace metals basis, Aldrich) before each experiment.

2.4. Film Preparation. MnOx catalyst films were prepared by controlled-potential electrolysis of solutions containing 0.5 mM Mn^{2+} and 50 mM methylphosphonate (MeP_i) at pH 8.0. These solutions remained clear over the course of all depositions. A FTO-coated glass slide was masked to 1 cm^2 and immersed in the quiescent solution. A constant potential of 0.537 V was applied to the electrode with automatic *iR* compensation until the total charge passed reached the desired loading of catalyst. For example, a 6 mC/cm^2 loading required ∼700 s of deposition time. Following deposition, films were immersed in reagent water to remove any trace Mn^{2+} and MeP_i remaining from solution. The films were prevented from drying by quickly transferring them to a Mn^{2+}-free solution for subsequent experiments.

2.5. Determination of Faradaic Efficiency. A fluorescence-based O_2 sensor (Ocean Optics) was employed to determine the Faradaic efficiency of oxygen evolution on MnOx. The total charge passed and the amount of O_2 detected by the sensor over time was recorded and is plotted in Figure S1 in the Supporting Information (SI). The experimental setup employed a custom-built, two-compartment, gastight electrochemical cell with a 14/20 port on each compartment and a Schlenk connection with a Teflon valve on the working compartment. One compartment contained a Pt mesh auxiliary electrode, and the other compartment contained the working and Ag/AgCl reference electrodes. The working electrode consisted of a 10 mC/cm^2 MnOx film electrodeposited on an FTO plate masked with Scotch tape to a 21.5 cm^2 area. The film was operated at 0.3 mA in 0.10 M P_i with 1.75 M KNO_3 electrolyte solution at pH 2.5, 7.0, and 12.0. Prior to measurements, the solution was degassed by bubbling with high purity Ar for 2 h with vigorous stirring. The 14/20 port of the working compartment was fitted with a FOXY OR125-73 mm O_2 sensing probe connected to a multi-frequency phase fluorometer. The phase shift of the O_2 sensor on the FOXY probe was recorded at 2 s intervals and then converted into the partial pressure of O_2 in the headspace using a two-point calibration curve (air, 20.9% O_2; and high purity Ar, 0% O_2). Because the amount of dissolved O_2 was small compared to the amount of generated O_2, no correction of the partial pressures by Henry's law was performed. These pressures were converted using the ideal gas law into O_2 concentration and compared to the theoretical yield of O_2, calculated by dividing the charge passed by 4*F*.

2.6. Electron Microscopy. Field emission scanning electron microscopy (FESEM) was performed on a 100 mC/cm^2 MnOx film electrodeposited on FTO (Figure S4 in the SI). The FESEM instrument (Zeiss Supra55VP) was operated at a beam voltage of 15.0 kV and at a working distance of ∼11 mm with a 30 μm aperture. InLens was used as the detector.

2.7. Tafel Data Collection. The current−voltage (Tafel) properties of the catalyst film in the region of oxygen evolution were measured by controlled potential electrolysis of 6 mC/cm^2 MnOx films in stirred Mn^{2+}-free solutions of 0.10 M P_i buffer in acidic (pH 1.0−3.5, Figure S2a in the SI), neutral (pH 5.5−8.5, Figure S2b in the SI), and alkaline (pH 11.35−13.30, Figure S2c in the SI) regimes. All solutions contained 1.73 M KNO_3 supporting electrolyte to achieve a high μ. The steady-state OER current density (j) was determined as a function of the applied overpotential (η) for freshly prepared 6 mC/cm^2 MnOx (a summary of the plots is shown in Figure 1). The solution was stirred at ∼600 rpm with a Teflon stir bar, and Tafel data were collected by adjusting the electrode potential from high to low values, in fixed mV decrements, across the linear Tafel

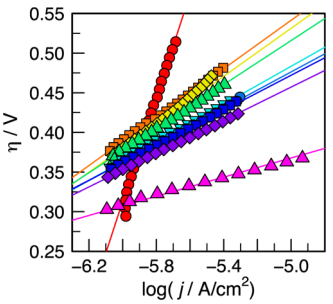

Figure 1. Tafel plots of the OER on 6 mC/cm^2 MnOx operating in 0.10 M P_i and 1.73 M KNO_3 at low pH 2.5 (red, ●); intermediate pH 5.5 (orange, ■), 6.0 (yellow, ◆), 6.5 (green, ▲), 7.0 (light blue, ▼), 7.5 (blue, ●), 8.0 (dark blue, ■), and 8.5 (purple, ◆); and high pH 12.0 (magenta, ▲). The overpotential (η) was used instead of E so that plots at different pHs could be displayed on the same scale. Intermediate pH plots have slopes that vary from 153 to 105 mV/decade, centered around 127 mV/decade at pH 7.0. The accessible range of potentials (and current densities) was restricted by corrosion at high potentials in some electrolyte conditions.

dx.doi.org/10.1021/ja413147e | J. Am. Chem. Soc. 2014, 136, 6002−6010

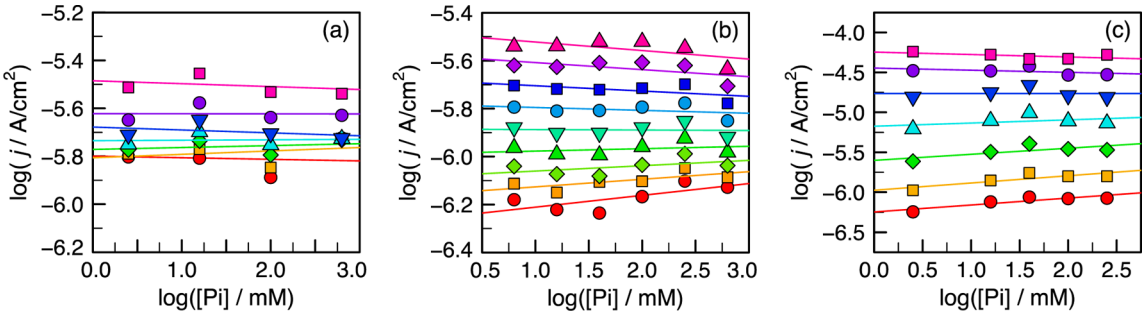

Figure 2. [P_i] dependence for the OER on MnOx (6 mC/cm^2 films) operated over a wide pH range at (a) pH 2.5 for E = 1.467 (red, ●), 1.497 (orange, ■), 1.527 (light green, ◆), 1.557 (light blue ▲), 1.587 (dark blue ▼), 1.617 (purple ●), and 1.647 V (magenta ■); (b) pH 7.0 for E = 0.960 (red ●), 0.970 (orange ■), 0.980 (light green ◆), 0.990 (green ▲), 1.000 (blue green ▼), 1.010 (blue ●), 1.020 (dark blue ■), 1.030 (violet ◆), and 1.040 V (magenta ▲); and (c) pH 12.5 for E = 0.777 (red ●), 0.792 (orange ■), 0.807 (green ◆), 0.822 (light blue ▲), 0.837 (dark blue ▼), 0.852 (purple ●), and 0.867 V (magenta ■) with varying P_i concentrations from 2.5 to 631.0 mM. In all solutions, appropriate amounts of KNO_3 were added to achieve a total ionic strength of 2 M. Data were interpolated at fixed potentials from Tafel plots in Figure S5 in the SI. The average slope in all three plots is zero.

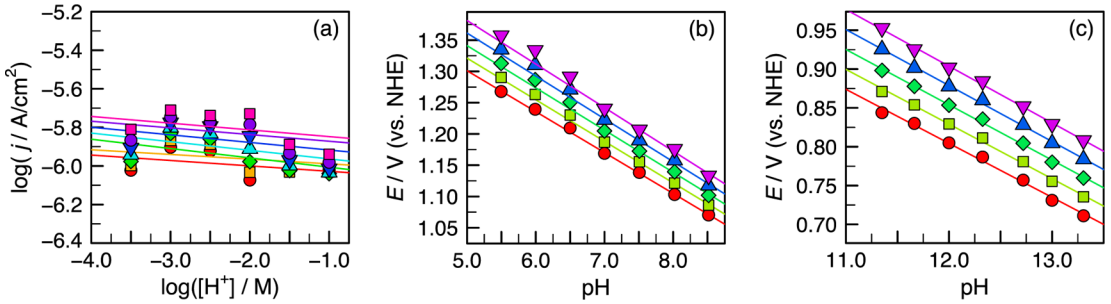

Figure 3. pH dependence for the OER on MnOx (6 mC/cm^2 films) operated in 0.10 M P_i and 1.73 M KNO_3 at (a) acidic pH 1.0 to 3.5, at E = 1.447 (red ●), 1.467 (orange ■), 1.487 (green ◆), 1.507 (light blue ▲), 1.527 (dark blue ▼), 1.547 (purple ●), and 1.567 V (magenta ■); (b) neutral pH 5.5 to 8.5, at log j = −6.10 (red ●), −5.95 (light green ■), −5.80 (green ◆), −5.65 (blue ▲), and −5.50 (magenta ▼); and (c) alkaline pH 11.35 to 13.30, at log j = −6.4 (red ●), −6.0 (light green ■), −5.6 (green ◆), −5.2 (blue ▲), and −4.8 (magenta ▼). Data were interpolated at fixed potentials in (a) and at constant current densities in (b) and (c) from Tafel data in Figure S2 in the SI. The average slope is (a) zero for proton concentration dependence from pH 1.0 to 3.5; (b) −67.5 ± 1.7 mV/pH for E/pH from pH 5.5 to 8.5; and (c) −71.3 ± 1.4 mV/pH for E/pH from pH 11.35 to 13.30.

region. At each potential, data were collected for 60−90 s such that steady-state current density was reached. To minimize any pseudocapacitance, the highest potential (first point in the sweep) was held for 30 min. Solution resistance was measured prior to data collection and automatically compensated. Tafel data collected in succession using the same and different electrodes exhibited good reproducibility and were not dependent on the direction of the potential scan. Performing the same experiments on blank FTO electrodes yielded current densities at least 1 order of magnitude lower than for FTO electrodes coated with a MnOx film, demonstrating low background contribution. Because the concentration of water is ∼55 M and well-buffered solutions were used, it was possible to collect activation-controlled current density without the necessity of using a rotating disk electrode (RDE) and attendant Koutecký−Levich (K−L) analysis. Nonetheless, control experiments comparing the Tafel slopes for plots collected on stirred solutions, using a RDE at 2500 rpm, and RDE coupled to K−L analysis established that stirring the solution with a stir bar at ∼600 rpm was sufficient to mitigate mass transport effects (Figure S8 in the SI). Film loading studies were performed on MnOx films of varying thicknesses by constant potential deposition on FTO, as described above, with passage of 0.5−500 mC/cm^2 charge and transferred to the Mn^{2+}-free electrolyte without drying (Figure S3 in the SI).

2.8. Phosphate Concentration Dependence. The dependence of P_i concentration on OER activity at pH 2.5, 7.0, and 12.5 was examined by recording Tafel plots on 6 mC/cm^2 MnOx films in stirred solutions at fixed pH of varying [P_i]: 2.5, 15.9, 100.0, and 631.0 mM at pH 2.5; 2.5, 6.3, 15.9, 39.9, 100.0, 251.2, and 631.0 mM at pH 7.0; and 2.5, 15.9, 39.8, 100.0, and 251.2 mM at pH 12.5 (Figure S5 in the SI). All solutions included KNO_3 to maintain a constant μ = 2.0 M so that the pK_a's of phosphoric acid could be accurately established. The data were interpolated at potentials from 1.467 to 1.647 V, incrementing by 30 mV at pH 2.5; 0.960 to 1.040 V, incrementing by 10 mV at pH 7.0; and 0.777 to 0.867 V, incrementing by 15 mV at pH 12.5, by slicing horizontally across the linear Tafel plots, to yield the dependence of activation current density (j_{ac}) on [P_i] (Figure 2).

A fixed ionic strength μ = 2 M was required to reliably prepare solutions of known [P_i]. Equilibrium constants were determined for μ = 2 M with KNO_3 as a supporting electrolyte. The reported pK_a's for phosphoric acid are 2.148, 7.198, and 12.375 at 25 °C.[49−51] An adjusted pK_a for P_i was calculated using specific ion interaction theory (SIT),[52] as implemented in the program *Ionic Strength Corrections using Specific Interaction Theory* (v 2.0);[53] the cation SIT parameter for H^+ (0.07) and the anion SIT parameters for $H_2PO_4^{2-}$ (−0.14), HPO_4^{2-} (−0.10), and PO_4^{3-} (−0.09 with a complex SIT parameter of −0.10) furnished corrected pK_a values of 1.582, 6.251, and 11.185 for electrolytes at μ = 2 M. These pK_a values were then used to calculate the speciation of P_i at various concentrations and to determine the amount of KNO_3 required to achieve the target value of μ = 2 M.

2.9. pH Dependence. The dependence of OER activity on pH was determined by constructing Tafel plots for MnOx films deposited from 6 mC/cm^2 in 0.10 M P_i and 1.73 M KNO_3 solutions at pH values spanning 1.0 to 3.5, incremented by 0.5 in acidic conditions; from pH 5.5 to 8.5, incremented by 0.5 in near-neutral conditions; and from pH 11.35 to 13.30, incremented by about 0.25 in alkaline conditions (Figure S2 in the SI).

dx.doi.org/10.1021/ja413147e | J. Am. Chem. Soc. 2014, 136, 6002−6010

The data were interpolated for the acidic cases at fixed potentials of 1.447−1.567 V, in 20 mV increments. The resulting plot presents the dependence of j_{ac} on proton concentration (Figure 3a). The intermediate and alkaline pH cases were interpolated at values of $\log(j_{ac})$: −6.10 to −5.50, in increments of 0.05 at intermediate pH; and −6.4 to −4.8, in 0.4 increments at alkaline pH, to yield the dependence of applied potential on pH (b and c of Figure 3). The slope of E vs. pH plots was multiplied by the negative reciprocal of the Tafel slope to extract the reaction order in pH.

The pH dependence at intermediate pH was also explored by potentiostatic titration of a 6 mC/cm^2 film in 0.10 M P_i and 1.73 M KNO_3 solution. The electrode was operated at a constant potential of 1.30 V, and the steady-state current density (measured after operation for ≥2 min at each pH) was recorded as the pH of the solution (measured *in situ*) was raised in increments of about 0.25 pH units using μL aliquots of 1 M KOH solution from pH 4 to pH 10. The plot of steady-state current density as a function of pH (Figure S6 in the SI) has a slope of 0.44 from pH 6 to 10. Below pH 6, the slope gradually decreases to zero.

2.10. Catalyst Tracking. The kinetic stability of MnOx films was evaluated by ^{31}P NMR where high-spin Mn^{2+} induces paramagnetic line broadening of the ^{31}P NMR signal of phosphate. Chronopotentiometry at 0 (open circuit) and 10 μA/cm^2 was performed on 100 mC/cm^2 MnOx films immersed in rapidly stirred solutions of increasing acidity: 0.10 M P_i with 1.90 M KNO_3 at pH 2.0, 4 M phosphoric acid at pH 0.1, and 4 M HCl with 0.10 M P_i at pH ∼−0.5. Aliquots of the electrolyte solution were sampled every 15 min over the course of 1 h. The Mn^{2+} concentration in each aliquot was quantified by measuring the full-width at half-maximum (fwhm) of the ^{31}P NMR signal for inorganic phosphate in the electrolyte. The magnitude of the broadening is directly proportional to the Mn^{2+} concentration. To produce calibration curves (Figure S7 in the SI), small precalculated microliter amounts of Mn^{2+} were added from a 0.5 mM stock to each electrolyte solution examined, producing solutions of known Mn^{2+} concentrations from 0 to 40 μM, in increments of 10 μM. Since the width of the ^{31}P NMR signal was highly sensitive to instrumental variables, data for the calibration curves were recorded immediately prior to those for the experimental samples in all cases. The measured concentrations were normalized against a fully dissolved 100 mC/cm^2 film ([Mn^{2+}] = 7.45 μM) to track the fractional dissolution of the film over time (Figure 4).

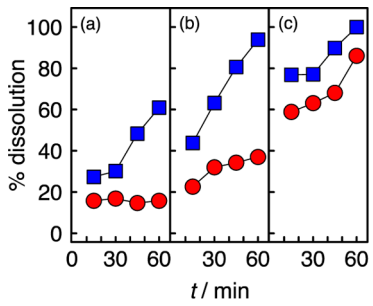

Figure 4. Percent of 100 mC/cm^2 MnOx film dissolved as a function of time (t) for application of 0 (blue, ■) and 10 (red, ●) μA/cm^2 current density in (a) 0.10 M P_i with 1.90 M KNO_3 solution at pH 2.0; (b) 4 M phosphoric acid at pH 0.1; and (c) 4 M HCl with 0.10 M P_i at pH −0.5. Lines are presented as guides.

3. RESULTS

MnOx films were prepared following procedures previously described for MnOx catalyst deposition.[54] FTO-coated glass slides, with 1 cm^2 working area, were polarized at a constant potential of 0.54 V (vs NHE) in quiescent solutions containing 0.5 mM Mn^{2+} and 50 mM MeP_i at pH 8.0. Deposition times varied, depending on the desired amount of catalyst deposited, but default catalyst loadings were 6 mC/cm^2 unless otherwise specified.

Figure S1 in the SI shows the total charge passed and the amount of O_2 detected by a fluorescent-based O_2 sensor. All current passed during the OER can be attributed to O_2 production. No degradation of the catalyst was detected, indicating that the OER Faradaic efficiency of MnOx is unity.

3.1. Tafel Analysis. The Tafel behavior of the OER of MnOx was measured by collecting steady-state current density (j) as a function of the applied overpotential (η) in acidic, neutral, and alkaline regimes of phosphate-buffered electrolyte (Figures 1 and S2 in the SI). Tafel plots in all pH regimes were reproducible under independent runs and were not dependent on the direction of the potential scan, indicating that the films were not altered during data collection. In acidic conditions, the Tafel plots possessed high slopes, over a range of 365−851 mV/decade with an average slope of 653 ± 166 mV/decade (Figure S2a in the SI). Under alkaline pH, the Tafel plots displayed linearity over two decades of current density with an average slope of 60.3 ± 2.9 mV/decade (Figure S2c in the SI). In addition, the Tafel slope remained close to 60 mV/decade over the entire alkaline pH range. At intermediate pHs, Tafel plots had an average slope of 127.4 ± 20.0 mV/decade (Figure S2b in the SI). Closer inspection revealed that the Tafel slopes systematically decreased with increasing pH. For example, Tafel slopes of 152.6, 119.9, and 104.9 mV/decade were observed for pH 5.5, 7.0 and 8.5, respectively.

Thicker MnOx films exhibited greater activities than thinner films, as evidenced by the monotonic shift of the Tafel plots to higher current densities with increased catalyst loadings. These data are shown in Figure S3 in the SI for films deposited with passage of charge from 0.5 to 500 mC/cm^2. Tafel slopes were preserved over a wide range of film thicknesses, indicating that the MnOx films are porous. This contention was supported by SEM images of thick films, which exhibited disc-like features (Figure S4 in the SI). Nonetheless, the activity of films thicker than 32 mC/cm^2 does not scale linearly with increased catalyst loadings. This is consistent with intrinsic limitations associated with proton−electron transport in porous OEC films.[55] In addition, upward bending of the Tafel plot occurred at high catalyst loadings. For these reasons, subsequent studies focus on the behavior of films deposited upon the passage of 6 mC/cm^2 under relatively well-buffered conditions, such that the films behave, in effect, as active sites that are equally accessible by an electric field from the electrode substrate, and may be treated using conventional electrokinetics theory.

3.2. Reaction Order Analysis. The reaction order (ρ) of a species at concentration c_i may be determined from electrokinetic measurements when the concentration of all other species ($c_{k\neq i}$) are held constant, and is given by

$$\rho = \left(\frac{\partial \log v}{\partial \log c_i}\right)_{c_{k\neq i}} = \left(\frac{\partial \log j}{\partial \log c_i}\right)_{c_{k\neq i}} \quad (1)$$

where the rate of the reaction, v, is directly proportional to the current density (j) driving the reaction.[56] Consequently, the reaction order of a species can be determined electrochemically by the slope of a log j vs log [c_i] plot at fixed potentials.

Tafel plots were collected at fixed pH while varying the concentration of phosphate, [P_i], to delineate the phosphate dependence of the OER activity of MnOx (Figure S5 in the SI). Horizontal interpolation of the Tafel data at constant potentials resulted in log j vs log [P_i] plots where the slope provided a

dx.doi.org/10.1021/ja413147e | J. Am. Chem. Soc. 2014, 136, 6002−6010

direct measure of P_i reaction order (Figure 2). The observed current densities in Figure 2, in acidic, neutral, and alkaline pH regimes, do not change appreciably over 2.5 magnitudes of $[P_i]$, indicating a zeroth-order dependence on $[P_i]$.

Similarly, the pH dependence of oxygen evolution on MnOx films was investigated by acquiring Tafel data over a pH range at constant $[P_i]$ (Figure S2 in the SI). At acidic pH, the OER activity did not significantly change over four pH units. Indeed, horizontal interpolation of the lower linear region ($E < 1.6$ V) of the Tafel plots at fixed potentials, yielded a zeroth-order dependence on proton concentration (Figure 3a) in acidic conditions.

In the alkaline regime, the Tafel slopes are lower, owing to the greater activity of MnOx in this pH range (Figure S2c in the SI). Consequently, a single "horizontal" slice through all data cannot encompass all Tafel plots. However, vertical interpolation of Tafel plots at fixed current densities yields the pH dependence of the steady-state potential at constant current density $(\partial E/\partial \mathrm{pH})_j$. The reaction order in pH (ρ_{pH}) may then be determined from the following partial derivative:[56]

$$\rho_{\mathrm{pH}} = \left(\frac{\partial \log j}{\partial \mathrm{pH}}\right)_E = -\left(\frac{\partial E}{\partial \mathrm{pH}}\right)_j \Big/ \left(\frac{\partial E}{\partial \log j}\right)_{\mathrm{pH}} \quad (2)$$

Thus, ρ_{pH} is furnished by dividing the negative of the slope of the potential vs pH plot by the Tafel slope. Applying this procedure to the data of Figure S2c in the SI by vertical interpolation of the Tafel plots at fixed current densities produces a potential vs pH plot with an average slope of −71.3 ± 1.4 mV/pH (Figure 3c). Dividing by the average Tafel slope furnishes a reaction order in pH of 1.2 ± 0.1. Therefore, oxygen evolution by MnOx exhibits an inverse first-order dependence on $[H^+]$ under alkaline conditions.

Applying the same procedure on data collected at intermediate pH (Figure S2b in the SI), vertical interpolation of the Tafel plots at fixed current densities resulted in a potential vs pH plot with an average slope of −67.5 ± 1.7 mV/pH (Figure 3b). Per eq 2, dividing by the negative of the average Tafel slope yielded an apparent reaction order in pH of 0.5 ± 0.2, which implies an inverse half-order in $[H^+]$. This fractional pH dependence at intermediate pH was explored further by potentiometric titration of the films from pH 6 to 10. In the titration, the potential was held constant at 1.3 V while the pH of the solution was slowly adjusted by increments of ∼0.05 units, which correspondingly caused an increase in current density. The solution was stirred rapidly, and sufficient time (1−5 min) was permitted for the current density to reach a steady-state value. The resulting log j vs pH plot was linear over four orders of pH; consequently, the slope of this plot directly yields the pH reaction order (Figure S6 in the SI). Consistent with the data of Figure 3b, a pH reaction order of 0.44 is obtained.

3.3. Film Dissolution Analysis. The kinetic stability of MnOx films at low pH was evaluated by measuring the Mn^{2+}-induced paramagnetic line broadening of the ^{31}P NMR peak for inorganic phosphate. MnOx films exhibit high intrinsic stability in intermediate and alkaline pH regimes; however, the degradation rate of MnOx films increases for more acidic solutions. Figure 4 shows the percent dissolution of MnOx films over time in the presence and absence of applied current (at fixed potential) at very acidic pHs (<2). Generally, films held at open circuit were less stable and dissolved more quickly than films operated at 10 μA/cm^2. As Figure 4a demonstrates, catalyst films operated in solutions of pH 2.0 were stable, and negligible dissolution of the films was observed when operated at 10 μA/cm^2. Conversely, removal of applied potential (i.e., no current) led to degradation of the film within an hour. Similarly, electrolysis of MnOx in the pH 0.1 solution exhibited significantly diminished dissolution compared to films held at open circuit (Figure 4b). Only in 4 M HCl (pH approximately −0.5) did the catalyst completely dissolve during operation of the film (Figure 4c).

4. DISCUSSION

The Faradaic efficiency measurements of Figure S1 in the SI establish that the observed current density originates solely from the production of O_2 by OER. To ensure that electrokinetics measurements reliably and reproducibly reflect this OER process, Tafel data must be collected for an activation-controlled reaction at the electrode. A series of experiments was performed to define the experimental conditions that were appropriate for such an activation-controlled OER process.

First, measured current densities must be unencumbered by the mass-transport of reactant to and product from the electrode. Whereas water is readily available as a reactant, even in in quiescent solutions, the production of protons resulting from OER can result in a local pH gradient, which can convolute the collection of Tafel data. To minimize the possibility of mass transport limitations associated with a pH gradient, solutions were stirred during the collection of Tafel data. To confirm that solutions were stirred sufficiently to enable an activation-controlled current to be collected, a series of Tafel plots were constructed for (i) MnOx on a stationary FTO electrode immersed in a stirred (Teflon stir bar at 600 rpm) solution, (ii) MnOx on a Pt RDE rotated at 2500 rpm, and (iii) MnOx on a Pt RDE at "infinite" rotational velocity as ascertained from a Koutecký−Levich (K−L) analysis (Figure S8 in the SI). The Tafel slopes were similar (∼120 mV/decade for P_i electrolyte at pH 7.0) and reproducible in all three cases. These results indicate that Tafel data could be collected for stirred solutions in an activation-controlled regime.

Second, capacitive contributions to the observed current density must also be minimal for constructing accurate Tafel plots of the OER process. Upon application of potential, the first few seconds of measured current density that rapidly decays can be ascribed to non-Faradaic current arising from the charging of the double-layer capacitance. Accordingly, current measurements were made in temporal domains beyond this short time scale window. However, additional pesudocapacitive effects over a longer time scale may arise from surface adsorption, intercalation of electrolyte anions, and/or surface structure changes.[56] Therefore, to reach steady-state conditions: (i) freshly deposited MnOx films were preanodized for at least 30 min in the same electrolyte used for subsequent Tafel analysis, and (ii) current density was measured over 30 to 60 s at each potential during Tafel data collection. The combination of both procedures yielded reproducible current densities with minimal capacitance contributions.

In addition, the Tafel behavior of MnOx films of varying thickness was examined. MnOx films were deposited with passage of charge ranging from 0.5 to 500 mC/cm^2 and operated in acidic and neutral P_i solutions (Figure S3 in the SI). As expected, thicker films had greater activities, as evidenced by the shift of the Tafel plot to higher current densities for increased catalyst loadings. Furthermore, Tafel slopes remained

dx.doi.org/10.1021/ja413147e | J. Am. Chem. Soc. 2014, 136, 6002−6010

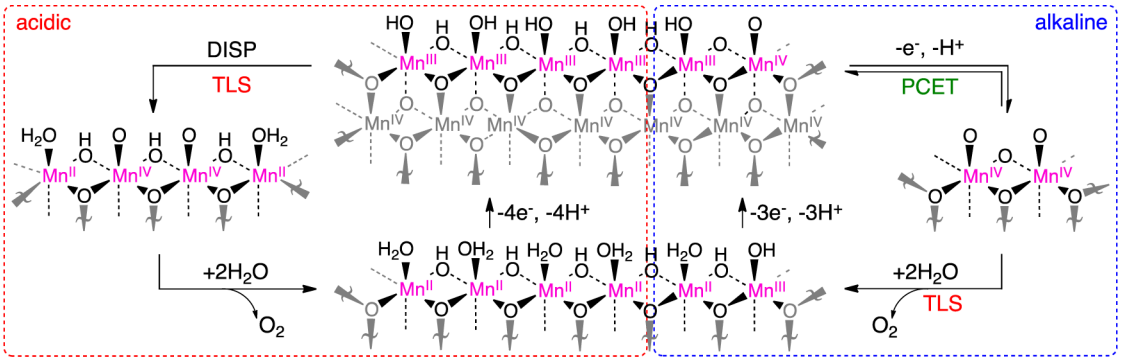

Figure 5. Proposed mechanism for the OER on MnOx in (left) acidic and (right) alkaline pH conditions. In the acidic regime, the resting state composed of Mn^{III} edge sites undergo turnover-limiting cross-site proton-coupled disproportionation to produce adjacent Mn^{IV} sites with terminal oxos. These terminal oxos couple to release O_2. In the alkaline regime, the mixed valent $Mn^{III/IV}$ resting state proceeds through a one-electron, one-proton PCET to generate adjacent Mn^{IV}=O sites. Similarly, these terminal oxos then couple in the turnover-limiting step to produce O_2.

the same over a wide range of film thicknesses (from 0.5 to 250 mC/cm^2) for the same pH. These observations suggest that the electrodeposited MnOx catalyst film is porous, as confirmed by the observation of disc-like structures in the SEM images of a thick film (Figure S4 in the SI). However, the increase in activity did not scale linearly as a function of loading owing to a limit that we have shown is intrinsic to such porous OEC films where proton−electron/hole transport necessarily exists in competition with the consumption of holes in catalytic reactions.[55] In materials such as these, an optimal/critical thickness is reached where electrode activity reaches a plateau. Therefore, thin films deposited with passage of 6 mC/cm^2 were selected for electrochemical measurements since they offered sufficient film thickness while preserving linear Tafel slopes across a wide potential range.

4.1. OER Rate Law in Alkaline Medium. The steady-state water oxidation mechanism of MnOx was initially interrogated using Tafel and reaction order plots at alkaline and acidic pH. In alkaline conditions from pH 11.35 to 13.30, the OER on MnOx exhibits average Tafel slopes of about 60 mV/decade with low deviation, zeroth-order dependence on $[P_i]$ (Figures 2c and S5c in the SI) and inverse first-order dependence on $[H^+]$ (Figures 3c and S2c in the SI). The electrochemical rate law for alkaline oxygen evolution on MnOx is

$$j_{\text{alkaline}} = j_{0,b}\exp\left[\frac{F\eta}{RT}\right] = 4Fk_0[H^+]^{-1}\exp\left[\frac{F\eta}{RT}\right] \quad (3)$$

where $j_{0,b}$ is the exchange current density, k_0 is the heterogeneous electrochemical rate constant at the reversible potential with units of (mol M)/(s cm^2), and 2.3 × RT/F denotes the 59 mV/decade Tafel slope. A Tafel slope close to 59 mV/decade is consistent with a one-electron pre-equilibrium preceding a turnover-limiting chemical step.[56]

Armed with the electrochemical rate law, a mechanistic model for the OER on MnOx under alkaline pH may be constructed with insights into catalyst resting state. Our work on oxidic metal films indicated that edge sites are particularly important for engendering catalysis.[24,25,57,58] In particular, two critical structural and chemical features of the resting state involve the identity of the oxygen ligands and the oxidation state of manganese at edge sites of MnOx in alkaline conditions.

The nature of the manganese oxidation state is furnished by prior coulometric measurements and XAS studies. Our previous coulometry analysis indicates an average oxidation state of +3.68 for Mn in MnOx;[54] thus, manganese exists in Mn^{III} and Mn^{IV} formal oxidation states. This result is consistent with the stoichiometric composition of $MnO_{1.7-2.0}$ that defines manganese dioxides.[59] Recent *in situ* X-ray absorption (XAS) and UV−vis spectroscopic studies also support the presence of Mn^{III} at the surface of active MnO_2 catalyst films.[37−44] We thus surmise that the resting state of MnOx consists of some Mn^{III}, in addition to Mn^{IV}, at edge sites. *Ex situ* XAS of MnO_2 films electrodeposited under conditions similar to those reported here, at constant potential from aqueous solutions of Mn^{2+} buffered with acetate at pH 6, suggest that these films comprise a pyrolusite material with a short-range structure that exhibits birnessite-like edge-sharing Mn octahedra. The pyrolusite polymorph of MnO_2 has a point of zero charge (PZC) of ~7.[60−62] By definition, at electrolyte pH below the PZC, the surface of the catalyst is positively charged and terminated predominantly by protonated oxygen in the form of bound water molecules and bridging hydroxyl groups. Above the PZC, the surface is negatively charged and is more likely to consist of terminal or bridging di-μ-oxo's. Therefore, in the alkaline regime from pH 11.35 to 13.30, the MnOx surface has partial negative charge, implying a preponderance of terminal hydroxo and oxo groups.

Figure 5 shows a model of MnOx in alkaline solution (blue dashed box) that is consistent with the structural and chemical characteristics of MnOx and the electrokinetics measurements. In the resting state, Mn^{III}−OH is converted to Mn^{IV}=O via a one-electron and one-proton PCET pre-equilibrium. This is followed by the chemical turnover-limiting step (TLS), which is likely O_2 liberation from coupling two adjacent terminal oxygen atoms. Such electrochemical behavior resembles that observed for Co−OEC, which also exhibits a PCET pre-equilibrium from a $Co^{III/IV}$ resting state preceding a chemical TLS step to furnish O_2.

4.2. OER Rate Law in Acidic Medium. In acidic conditions from pH 1.0 to 3.5, the Tafel plots exhibited a high average slope of about 653 mV/decade, zeroth-order dependence on $[P_i]$ (Figures 2a and S5a in the SI), and zeroth-order dependence on $[H^+]$ (Figures 3a and S2a in the SI). Slopes much greater than 120 mV/decade are classified as quasi-infinite and are consistent with an initial turnover-limiting chemical step.[56] The electrochemical rate law for acidic OER on MnOx is then simply:

$$j_{\text{acidic}} = j_{0,a} \quad (4)$$

dx.doi.org/10.1021/ja413147e | J. Am. Chem. Soc. 2014, 136, 6002−6010

where $j_{0,a}$ is the potential independent exchange current density.

Possible chemical steps include O−O bond formation, O_2 liberation, deprotonation of surface hydroxyls by water, or disproportionation of surface Mn^{3+}. However, assigning the TLS to O−O bond formation or O_2 liberation is unlikely because both of these steps require that the resting state of the catalyst surface is fully composed of reactive terminal Mn^{IV}=O, which is inconsistent with the observed average Mn oxidation state, PZC of MnOx, and recent literature, all of which suggest the presence of Mn^{3+} in active manganese oxide water oxidation catalysts. Furthermore, in acidic conditions, bridging di-μ-hydroxyl and terminal hydroxyl groups—not terminal oxos—are favored, and thus OER formation would have to be accompanied by PCET to the electrode, which cannot generally be accommodated by an infinite Tafel slope.

Hence, the remaining possibilities are deprotonation of surface hydroxyls by water and disproportionation of surface-bound Mn^{III}. Considering the former case, there are two possible proton acceptors under acidic conditions: water and adjacent Mn^{III}−OH sites. Given that the pK_a of H_3O^+ is −1.7[63] and that of Mn^{III}−OH_2^+ (from manganite, for comparison) is 5.72,[64] it is significantly more favorable to perform a surface proton transfer to create adjacent Mn^{III}−OH_2^+ and Mn^{III}−O^- groups, which are then poised to disproportionate. Indeed, surface-bound Mn^{3+} oxides have a large equilibrium constant for disproportionation under acidic conditions,[65] as recently observed by Takashima et al.[38] However, on the surface, the disproportionation is likely coupled with a cross-site proton transfer which serves to limit the rate of the process due to the inversion of pK_a required to access Mn^{III}−OH_2^+ and Mn^{III}−O^- intermediates. A similar mechanism is observed in Meyer's surface-bound polypyridyl Ru complexes where two adjacent Ru^{III}−OH undergo proton transfer and disproportionation to form Ru^{II}−OH_2 and Ru^{IV}=O species.[66] Thus, assigning the TLS to a cross-site proton-coupled disproportionation is consistent with the observed Tafel and reaction order data in acidic electrolytes. Figure 5 (red dashed box) illustrates this model where four Mn^{III}−OH sites disproportionate to two Mn^{II}−OH_2 and two Mn^{IV}=O species. The adjacent Mn^{IV}=O sites may then couple terminal oxos and liberate O_2. Four adjacent Mn^{III} sites are needed to generate two neighboring Mn^{IV} sites. The likelihood of sampling a reaction coordinate possessing four contiguous Mn^{III} sites is likely to be small, and thus accounts for the low activity of MnOx in acidic solution.

4.3. OER Rate Law in Intermediate pH Medium. In neutral conditions at pH 7.0, MnOx displayed an average slope near 120 mV/decade (Figures 1 and S2b in the SI). Although this slope is characteristic of a first-step, turnover-limiting, electron transfer,[56] in this case, the Tafel slope varies systematically over the intermediate pH range from 153 mV/decade (at pH 5.5) to 105 mV/decade (at pH 8.5) and is observed over a narrow range of current density. That is, the 105−150 mV/decade Tafel slopes do not reflect the kinetics of a single mechanism at pH 7 but rather are consistent with a narrow regime displaying mixed-control by two reaction pathways. Thus, Langmuir conditions cannot be assumed.[56] Indeed, the catalyst films exhibit approximately inverse half-order fractional dependence on proton concentration (Figure 3b), which would result from the combination of zeroth-order $[H^+]$ dependence at acidic pH and inverse first-order $[H^+]$ dependence at alkaline pH. These observations suggest that, at intermediate pH, there are two primary competing pathways: (i) in acidic conditions, a disproportionation mechanism with zeroth-order dependence on proton concentration, and (ii) at alkaline pH, a one-electron, one-proton PCET mechanism. In this model, the pH of the electrolyte modulates the contribution of each mechanism. Assuming a surface-bound Mn^{3+} disproportionation reaction described in Figure 5, the propensity for the reaction to occur diminishes exponentially as pH increases. Thus, in alkaline conditions, there is no contribution from the disproportionation mechanism, while in the acidic regime, disproportionation is the dominant pathway. Our results are consistent with a similar conclusion reached by Takashima et al. where Mn^{III} is stabilized in alkaline electrolyte but disproportionate readily in acidic conditions.[41,44] An emerging trend establishes that OER is enhanced in manganese oxides when Mn^{3+} is introduced through voltage cycling protocols[28,31,35,37] or via chemical synthesis.[29,38,39,47] These studies reinforce the important role that Mn^{3+} plays in facilitating OER.

4.4. Stability and Self-Healing. The stability of MnOx and other metal oxide materials is generally considered within the context of the intrinsic thermodynamic and kinetics properties of the catalyst itself. Generally, the dissolution of metal ions from oxide materials correlates with ligand substitution rates in metal aquo complexes,[67] where the rate is dominated by the electron count of the metal in a given ligand field, most notably octahedral or pseudo-octahedral for metal oxide catalysts. Population of electrons in metal antibonding orbitals, especially in the e_g* set, diminish the metal−ligand bond order and promote substitutional lability.[9,68] Analogously in metal oxides, where both the t_{2g}* and e_g* orbitals of a local metal center are antibonding, increased d-electron counts and high-spin electron configurations weaken the metal−oxygen framework and lead to more facile oxide degradation. Thus, early first-row transition metal oxides, such as MnOx, are more intrinsically stable in contact with acids than are late first-row metal oxides with higher d-electron counts.

Notwithstanding, most metal oxides are also unstable under the conditions of OER. The four-electron chemistry of OER causes metals to cycle through a range of oxidation states. In the mechanism outlined in Figure 5, Mn^{2+} is attendant to O_2 evolution; the high-spin d^5 nature of Mn^{2+} imparts to it exceptional substitutional lability and accelerates the dissolution of the catalyst film. These electronic configurations are augmented by acid−base chemistry. In the case of oxides, acidic pH regimes are especially deleterious to catalyst stability. For these reasons, MnOx naturally leaches into solution in acidic electrolytes and during OER, as established by ^{31}P NMR line broadening experiments.

Though intrinsically unstable, MnOx and more generally, other anodically electrodeposited metal oxide films, may be functionally stable if a self-healing mechanism is introduced as part of the catalytic cycle. As long as MnOx deposition occurs at potentials below those required for OER, the films will remain stable through self-repair owing to the reoxidation of manganese ions in solution. A similar self-healing process has been recently inferred by Casey and Britt[47] during OER for manganese oxide in the presence of a chemical oxidant.

To better visualize the relation between deposition and OER kinetics processes, Tafel plots derived for growth and oxygen evolution on MnOx were combined and reformulated in terms of a single potential (E) vs pH plot (Figure 6). This plot incorporates the inverse first- and zeroth-order dependence on

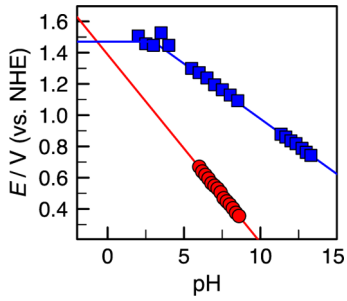

Figure 6. Potential dependence on pH for MnOx deposition (red, ●) and oxygen evolution on MnOx (blue, ■). Data were interpolated at j = 1.3 μA/cm^2 from Tafel plots for MnOx deposition (see ref 54) and OER (Figure S2 in the SI). The deposition trace is consistent with an inverse fourth-order dependence on [H$^+$] in the acidic regime[69] and assumes a Mn^{2+} solution concentration of 50 μM, which is consistent with concentrations for a dissolved 6 mC/cm^2 MnOx film.

[H$^+$] for the OER in the alkaline and acidic regimes, respectively, and the inverse fourth-order dependence on [H$^+$] for MnOx deposition near-neutral[54] to acidic[69] pH. The difference in proton order between deposition and oxygen evolution on MnOx results in the deposition potential rising faster than the OER potential as pH is lowered (for the same current density). Eventually, the two traces cross and mark the point where film repair can no longer keep pace with film degradation during the OER process. As indicated in Figure 6, this crossover emerges near pH 0 and provides a prediction of where self-healing ceases and net film dissolution manifests.

To test our prediction and quantify functional stability, film dissolution was examined with Mn^{2+}-induced paramagnetic line broadening of the ^{31}P NMR peak for inorganic phosphate in acidic solutions at pH 2.0, 0.1, and −0.5 (Figure 4). The catalyst displayed characteristics of both intrinsic and functional kinetic stability. The intrinsic stability prevented complete dissolution of the film even at pH 2.0 in the absence of applied current (Figure 4a). Additional stabilization of MnOx was obtained by self-healing the catalyst films and was exemplified by the significantly slower rate of dissolution and diminished overall percent dissolution for the system under operation in 4 M phosphoric acid (pH ≈ 0.1) compared to films held at open circuit (Figure 4b). However, it is only in 4 M HCl with a pH of approximately −0.5 that the operating catalyst films could finally no longer be stabilized and decayed with rate similar to those at open circuit with film dissolution (Figure 4c). These observations concur with the predictions of Figure 6.

5. CONCLUSION

Electrokinetic experiments on electrodeposited MnOx films were performed over a wide pH range (in acidic, neutral, and alkaline P$_i$ electrolytes) and revealed two competing mechanisms. In acidic conditions, a quasi-infinite Tafel slope and lack of proton dependence in the rate law indicated an initial chemical TLS that was assigned to surface Mn^{3+} disproportionation. At alkaline pH, an average Tafel slope of approximately 60 mV/decade contributed to a rate law concordant with a one-electron, one-proton PCET equilibrium preceding a turnover-limiting chemical step. At neutral pH, competition between these two mechanisms resulted in a half-order dependence on proton concentration and Tafel slopes that are intermediate to those observed for the limiting acidic and alkaline regimes.

A key feature that differentiates MnOx from other electrodeposited, late first-row transition metal oxides is its higher intrinsic and functional kinetic stability in acidic electrolytes. Although MnOx is not as catalytically active for OER as late metal oxidic films, such as Co−OEC and Ni−OEC, it is able to perform OER in very acidic environments owing to the increased inertness of MnOx and its ability to maintain self-healing for electrolytes with pH greater than zero. Our results show that self-healing may be predictably quantified by acquiring mechanistic knowledge of the interplay between OER and deposition electrokinetics, and thus self-healing may be incorporated as a general design principle in catalysis development, especially in expanding the operational range of OER catalysts.

■ ASSOCIATED CONTENT

Ⓢ Supporting Information

O_2 sensor measurements, Tafel plots, SEM images, and NMR line broadening calibration curves. This material is available free of charge via the Internet at http://pubs.acs.org.

■ AUTHOR INFORMATION

Corresponding Author

dnocera@fas.harvard.edu

Notes

The authors declare no competing financial interest.

■ ACKNOWLEDGMENTS

This research was supported by DOE DE-SC0009565. SEM imaging was performed at Harvard University's Center for Nanoscale Systems (CNS), a member of the National Nanotechnology Infrastructure Network (NNIN), which is supported by the National Science Foundation under ECS-0335765. We thank Casandra Cox for instruction on O_2 Faradaic efficiency measurement.

■ REFERENCES

(1) Lewis, N. S.; Nocera, D. G. *Proc. Natl. Acad. Sci. U.S.A.* **2006**, *103*, 15729−15735.
(2) Abbott, D. *Proc. IEEE* **2010**, *98*, 42−66.
(3) Hoffert, M. I.; Caldeira, K.; Jain, A. K.; Haites, E. F.; Harvey, L. D. D.; Potter, S. D.; Schlesinger, M. E.; Schneider, S. H.; Watts, R. G.; Wigley, T. M. L.; Wuebbles, D. J. *Nature* **1998**, *395*, 881−884.
(4) Nocera, D. G. *Inorg. Chem.* **2009**, *48*, 10001−10017.
(5) Cook, T. R.; Dogutan, D. K.; Reece, S. Y.; Surendranath, Y.; Teets, T. S.; Nocera, D. G. *Chem. Rev.* **2010**, *110*, 6474−6502.
(6) Barber, J. *Chem. Soc. Rev.* **2009**, *38*, 185−196.
(7) Cukier, R. I.; Nocera, D. G. *Annu. Rev. Phys. Chem.* **1998**, *49*, 337−369.
(8) Huynh, M. H. V.; Meyer, T. J. *Chem. Rev.* **2007**, *107*, 5004−5064.
(9) Betley, T. A.; Wu, Q.; Van Voorhis, T.; Nocera, D. G. *Inorg. Chem.* **2008**, *47*, 1849−1861.
(10) Eisenberg, R.; Gray, H. B. *Inorg. Chem.* **2008**, *47*, 1697−1699.
(11) Hernández-Pagán, E. A.; Vargas-Barbosa, N. M.; Wang, T.; Zhao, Y.; Smotkin, E. S.; Mallouk, T. E. *Energy Environ. Sci.* **2012**, *5*, 7582−7589.
(12) Rossmeisl, J.; Qu, Z.-W.; Zhu, H.; Kroes, G.-J.; Nørskov, J. K. *J. Electroanal. Chem.* **2007**, *607*, 83−89.
(13) Man, I. C.; Su, H.-Y.; Calle−Vallejo, F.; Hansen, H. A.; Martínez, J. I.; Inoglu, N. G.; Kitchin, J.; Jaramillo, T. F.; Nørskov, J. K.; Rossmeisl, J. *ChemCatChem.* **2011**, *3*, 1159−1165.
(14) Woodhouse, M.; Parkinson, B. A. *Chem. Soc. Rev.* **2009**, *38*, 197−210.
(15) Gerken, J. B.; Chen, J. Y. C.; Massé, R. C.; Powell, A. B.; Stahl, S. S. *Angew. Chem., Int. Ed.* **2012**, *51*, 6676−6680.

(16) Trasatti, S. In *The Electrochemistry of Novel Materials*; Lipkowski, J., Ross, P. N., Eds.; VCH: New York, 1994; pp 207−251.
(17) Surendranath, Y.; Nocera, D. G. *Prog. Inorg. Chem.* **2011**, *57*, 505−560.
(18) Lutterman, D. A.; Surendranath, Y.; Nocera, D. G. *J. Am. Chem. Soc.* **2009**, *131*, 3838−3839.
(19) Surendranath, Y.; Lutterman, D. A.; Liu, Y.; Nocera, D. G. *J. Am. Chem. Soc.* **2012**, *134*, 6326−6336.
(20) Nocera, D. G. *Acc. Chem. Res.* **2012**, *45*, 767−776.
(21) Surendranath, Y.; Bediako, D. K.; Nocera, D. G. *Proc. Natl. Acad. Sci. U.S.A.* **2012**, *109*, 15617−15621.
(22) Winkler, M. T.; Cox, C. R.; Nocera, D. G.; Buonassisi, T. *Proc. Natl. Acad. Sci. U.S.A.* **2013**, *110*, E1076−E1082.
(23) Kanan, M. W.; Nocera, D. G. *Science* **2008**, *321*, 1072−1075.
(24) Surendranath, Y.; Kanan, M. W.; Nocera, D. G. *J. Am. Chem. Soc.* **2010**, *132*, 16501−16509.
(25) Bediako, D. K.; Surendranath, Y.; Nocera, D. G. *J. Am. Chem. Soc.* **2013**, *135*, 3662−3674.
(26) Dincă, M.; Surendranath, Y.; Nocera, D. G. *Proc. Natl. Acad. Sci. U.S.A.* **2010**, *107*, 10337−10341.
(27) Revie, R. W., Ed. *Uhlig's Corrosion Handbook*, 3rd ed.; John Wiley: Hoboken, NJ, 2011.
(28) Zaharieva, I.; Chernev, P.; Risch, M.; Klingan, K.; Kohlhoff, M.; Fischer, A.; Dau, H. *Energy Environ. Sci.* **2012**, *5*, 7081−7089.
(29) Robinson, D. M.; Go, Y. B.; Mui, M.; Gardner, G.; Zhang, Z.; Mastrogiovanni, D.; Garfunkel, E.; Li, J.; Greenblatt, M.; Dismukes, G. C. *J. Am. Chem. Soc.* **2013**, *135*, 3494−3501.
(30) Bergmann, A.; Zaharieva, I.; Dau, H.; Strasser, P. *Energy Environ. Sci.* **2013**, *6*, 2745−2755.
(31) Hocking, R. K.; Brimblecombe, R.; Chang, L.-Y.; Singh, A.; Cheah, M. H.; Glover, C.; Casey, W. H.; Spiccia, L. *Nat. Chem.* **2011**, *3*, 461−466.
(32) Zhou, F.; Izgorodin, A.; Hocking, R. K.; Spiccia, L.; MacFarlane, D. R. *Adv. Energy Mater.* **2012**, *2*, 1013−1021.
(33) Fekete, M.; Hocking, R. K.; Chang, S. L. Y.; Italiano, C.; Patti, A. F.; Arena, F.; Spiccia, L. *Energy Environ. Sci.* **2013**, *6*, 2222−2232.
(34) Zhou, F.; Izgorodin, A.; Hocking, R. K.; Armel, V.; Spiccia, L.; Macfarlane, D. R. *ChemSusChem* **2013**, *6*, 643−651.
(35) Gorlin, Y.; Jaramillo, T. F. *J. Am. Chem. Soc.* **2010**, *132*, 13612−13164.
(36) Gorlin, Y.; Jaramillo, T. F. *J. Electrochem. Soc.* **2012**, *159*, H782−H786.
(37) Gorlin, Y.; Lassalle-Kaiser, B.; Benck, J. D.; Gul, S.; Webb, S. M.; Yachandra, V. K.; Yano, J.; Jaramillo, T. F. *J. Am. Chem. Soc.* **2013**, *135*, 8525−8534.
(38) Mette, K.; Bergmann, A.; Tessonnier, J.-P.; Hävecker, M.; Yao, L.; Ressler, T.; Schlögl, R.; Strasser, P.; Behrens, M. *ChemCatChem.* **2012**, *4*, 851−862.
(39) Bergmann, A.; Zaharieva, I.; Dau, H.; Strasser, P. *Energy Environ. Sci.* **2013**, *6*, 2745−2755.
(40) Ramírez, A.; Bogdanoff, P.; Friedrich, D.; Fiechter, S. *Nano Energy* **2012**, *1*, 282−289.
(41) Morita, M.; Iwakura, C.; Tamura, H. *Electrochim. Acta* **1977**, *22*, 325−328.
(42) Morita, M.; Iwakura, C.; Tamura, H. *Electrochim. Acta* **1979**, *24*, 357−362.
(43) Takashima, T.; Hashimoto, K.; Nakamura, R. *J. Am. Chem. Soc.* **2012**, *134*, 1519−1527.
(44) Takashima, T.; Hashimoto, K.; Nakamura, R. *J. Am. Chem. Soc.* **2012**, *134*, 18153−18156.
(45) Najafpour, M. M.; Leonard, K. C.; Fan, F.-R. F.; Tabrizi, M. A.; Bard, A. J.; King'ondu, C. K.; Suib, S. L.; Haghighi, B.; Allakhverdiev, S. I. *Dalton Trans.* **2013**, *42*, 5085−5091.
(46) Najafpour, M. M.; Sedigh, D. J. *Dalton Trans.* **2013**, *42*, 12173−12178.
(47) Najafpour, M. M.; Kompany-Zareh, M.; Zahraei, A.; Jafarian Sedigh, D.; Jaccard, H.; Khoshkam, M.; Britt, R. D.; Casey, W. H. *Dalton Trans.* **2013**, *42*, 14603−14611.
(48) Parsons, R. In *Advances in Electrochemistry and Electrochemical Engineering*; Delahay, P., Ed.; Interscience: New York, 1961; pp 1−64.
(49) Bates, R. G. *J. Res. Natl. Bur. Stand.* **1951**, *47*, 127−134.
(50) Bates, R. G.; Acree, S. F. *J. Res. Natl. Bur. Stand.* **1943**, *30*, 129−155.
(51) Vanderzee, C. E.; Quist, A. S. *J. Phys. Chem.* **1961**, *65*, 118−123.
(52) Grenthe, I.; Plyasunov, A. *Pure Appl. Chem.* **1997**, *69*, 951−958.
(53) Pettit, L. D.; Puigdomenech, I.; Wanner, H.; Sukhno, I.; Buzko, V. *Ionic Strength Corrections using Specific Interaction Theory*; 2008, http://old.iupac.org/projects/2006/2006-010-1-500.html (accessed Jan 12, 2013).
(54) Huynh, M.; Bediako, D. K.; Liu, Y.; Nocera, D. *J. Phys. Chem. C* **2014**, DOI: 10.1021/jp501768n.
(55) Bediako, D. K.; Costentin, C.; Jones, E. C.; Nocera, D. G.; Savéant, J.-M. *J. Am. Chem. Soc.* **2013**, *135*, 10492−10502.
(56) Gileadi, E. *Physical Electrochemistry: Fundamentals, Techniques and Applications*, 1st ed.; Wiley−VCH: Weinheim, 2011.
(57) Wang, L.-P.; Van Voorhis, T. *J. Phys. Chem. Lett.* **2011**, *2*, 2200−2204.
(58) Lee, S. W.; Carlton, C.; Risch, M.; Surendranath, Y.; Chen, S.; Furutsuki, S.; Yamada, A.; Nocera, D. G.; Shao-Horn, Y. *J. Am. Chem. Soc.* **2012**, *134*, 16959−16962.
(59) Pisarczyk, K. *Kirk−Othmer Encyclopedia of Chemical Technology*; John Wiley: New York, 1991; pp 501−532.
(60) Healy, T. W.; Herring, A. P.; Fuerstenau, D. W. *J. Colloid Interface Sci.* **1966**, *21*, 435−444.
(61) Gray, M. J.; Malati, M. A.; Rophael, M. W. *J. Electroanal. Chem. Interfac.* **1978**, *89*, 135−140.
(62) Chabre, Y.; Pannetier. *J. Prog. Sol. State Chem.* **1995**, *23*, 1−130.
(63) Jencks, W. P.; Regenstein, J. In *Handbook of Biochemistry and Molecular Biology*; Lundblad, R. L., MacDonald, F. M., Eds.; CRC Press: Boca Raton, FL, 2010; pp 595−635.
(64) Xyla, A. G.; Sulzberger, B.; Luther, G. W.; Hering, J. G.; Van Cappellen, P.; Stumm, W. *Langmuir* **1992**, *8*, 95−103.
(65) Batchelor-McAuley, C.; Shao, L.; Wildgoose, G. G.; Green, M. L. H.; Compton, R. G. *New J. Chem.* **2008**, *32*, 1195−1203.
(66) Chen, Z.; Vannucci, A. K.; Concepcion, J. J.; Jurss, J. W.; Meyer, T. J. *Proc. Natl. Acad. Sci. U.S.A.* **2011**, *108*, E1461−E1469.
(67) Casey, W. H. *J. Colloid Interface Sci.* **1991**, *146*, 586−589.
(68) Basolo, F.; Pearson, R. G. In *Mechanisms of Inorganic Reactions*; Wiley: New York, 1967.
(69) Fleischmann, M.; Thirsk, H. R.; Tordesillas, I. M. *Trans. Faraday Soc.* **1962**, *58*, 1865−1877.